Influence of idealized heterogeneity on wet and dry planetary boundary layers coupled to the land surface; I: Instantaneous fields and statistics

Edward G. Patton[1], Peter P. Sullivan, and Chin-Hoh Moeng

National Center for Atmospheric Research

[1] *Corresponding address:* Edward G. Patton, MMM Division, NCAR, P.O. Box 3000, Boulder, CO 80307-3000. *email:* patton@ucar.edu *phone:* 303-497-8958

Abstract

This is the first in a two-part series of manuscripts describing numerical experiments on the influence of 2-30 km strip-like heterogeneity on wet and dry boundary layers coupled to the land surface. The strip-like heterogeneity is shown to dramatically alter the structure of the free-convective boundary layer by inducing significant organized circulations that modify turbulent statistics. The coupling with the land-surface modifies the circulations compared to previous studies using fixed surface forcing. Total boundary layer turbulence kinetic energy increases significantly for surface heterogeneity at scales between $\lambda/z_i = 4$ and 9, however entrainment rates for all cases are largely unaffected by the strip-like heterogeneity.

1. Introduction

Land-atmosphere coupling is widely recognized as a crucial component of regional, continental and global scale numerical models. Predictions from these large-scale models are sensitive to small-scale surface layer processes like heat and moisture fluxes at the air-soil-vegetation interface as well as boundary layer treatments (*e.g.*, Garratt, 1993). The soil moisture boundary condition has a considerable influence on medium- to long-range weather forecasts and on simulated monthly mean climatic states (*e.g.*, Rowntree and Bolton, 1983). Heterogeneous soil moisture conditions can occur at many scales both naturally (Mahrt et al., 2001a) and through human modification (Weaver and Avissar, 2001). Naturally occurring heterogeneity can arise through a number of mechanisms such as spatially varying soil or vegetation type and human-induced heterogeneity can result from spatially-varying agricultural practices that vary from farmer to farmer. Both types of heterogeneity can introduce dramatic variability in boundary layer surface forcing.

There have been a number of prior investigations into the effects of non-homogeneous surface forcing on the PBL using high-resolution large eddy simulation (LES) (*e.g.*, Hechtel et al., 1990; Hadfield et al., 1991; Shen and Leclerc, 1995; Avissar and Schmidt, 1998; Albertson and Parlange, 1999; Albertson et al., 2001; Raasch and Harbusch, 2001; Esau and Lyons, 2002; Kustas and Albertson, 2003). Hechtel et al. (1990) used measurements to drive a relatively coarse resolution LES and found no significant modifications to homogeneous cases which they attributed to having a mean wind in their simulation. Hadfield et al. (1991) studied relatively small-scale (1.5 and 4.5 km wavelength) strip-like heterogeneity

under free convective conditions and found that the heterogeneity induced organized motions in the PBL. These motions increased horizontal and vertical velocity variances near the upper/lower boundaries and in the mid-PBL, respectively. Shen and Leclerc (1995) and Raasch and Harbusch (2001) showed that for small-scale patch-like heterogeneity, the intensity of the organized motions increased when the horizontal-scale of the heterogeneity increased to about the PBL height. When investigating land-surface forcing that is fixed in time, Avissar and Schmidt (1998) found larger-scale heterogeneity to continually intensify the organized motions when the heterogeneity increased from two to forty kilometers. Rather than specify the surface fluxes, which completely decouples the forcing from the overlying atmosphere, Albertson and Parlange (1999), Albertson et al. (2001), and Kustas and Albertson (2003) investigated land-surface heterogeneity using specified surface temperature and moisture. However, none of these studies used a dynamically coupled system where the soil responds to the atmosphere and vice versa. In addition, these studies are typically of relatively coarse resolution (12.5 m $\leq \Delta x \leq$ 100 m, and 20 m $\leq \Delta z \leq$ 50 m) and, with the exception of Avissar and Schmidt (1998), focused on relatively small-scale heterogeneity (*e.g.*, $250m \leq \lambda \leq 5km$). In our view, the shortcomings and sensitivities exhibited by large-scale numerical models are a consequence of both the inadequate modeling of the PBL and poor representation of the interaction with the land surface. In order to improve existing parameterizations, a more complete understanding of the mechanics and thermodynamics of air-soil interaction and the transport of water vapor by turbulent processes in the PBL are required.

This paper is the first of two manuscripts examining the interactions between the atmosphere and the land surface using an LES model for the PBL coupled to a land surface model (LSM). Fine grids and large computational domains are used to examine the impact of a range of soil heterogeneity scales (λ = 2-30 km) on PBL turbulence and the vertical flux of water vapor mixing ratio. The coupling between the PBL and the land-surface is found to be of fundamental importance in determining the PBL response. The heterogeneity is shown to influence the PBL differently depending on the moisture content of the PBL air. In the second manuscript (Patton et al., 2003b), the organized motions induced by the heterogeneity are described in detail through phase-averaged statistics.

2. Land-Atmosphere Coupling

Over land surfaces during daytime hours, the surface energy balance (SEB) is thermodynamically coupled to the growth of the boundary layer through interactions between the surface sensible and latent heat fluxes, the atmospheric temperature and humidity and the growth rate of the boundary layer by entrainment (Raupach, 2000). Through the SEB, incoming solar radiation absorbed at the ground is partitioned to determine the energy available to the coupled land-atmosphere system. Key entities involved in the SEB, such as heat and water vapor fluxes, are influenced by PBL concentrations of these quantities which themselves are influenced by their surface fluxes, forming a negative feedback loop (McNaughton and Raupach, 1996).

The main focus of this research is on the PBL, but in an attempt to incorporate these

important feedbacks in the study, we coupled our well-established 3D, time-dependent, LES code (Sullivan et al., 1996) to the NOAH (National Center for Environmental Prediction / Oregon State University / Air Force / Office of Hydrology) LSM, version 2.0 (Chang et al., 1999). Numerous models of varying sophistication and empiricism have been proposed to describe the physics of soil-water-vegetation systems. Our choice of the NOAH model is based on the following desirable features: 1) the straightforward manner with which it can be coupled with a parent atmospheric model, 2) only a few empirical constants are needed to describe the land surface, 3) its good predictive capabilities, and 4) the robustness of the model itself.

The LES predicts three-dimensional and time-dependent velocity fields (u, v, w) by numerically integrating a filtered set of incompressible Navier-Stokes equations under the Boussinesq approximation. To incorporate buoyancy effects, the LES also integrates a thermodynamic energy equation (θ) and an equation for water vapor mixing ratio (q), which are combined to calculate virtual potential temperature $(\theta_v = \theta + 0.61\theta q)$. The effects of unresolved motions in the LES are estimated by following an equation for subgrid-scale (SGS) energy (e). In the soil, the LSM (NOAH) predicts vertical profiles of temperature (T) and moisture (Θ), by integrating a 1-D set of the soil thermodynamic and hydrologic equations (Mahrt and Pan, 1984; Pan and Mahrt, 1987). At every (x,y) grid point, the lower boundary conditions for the LES and the upper boundary conditions for the LSM define the coupling between the PBL and the land-surface. Atmospheric velocity boundary conditions are determined through dynamically calculating a drag coefficient from a prescribed surface

roughness length and the wind field at the first LES grid level, while surface temperature and moisture boundary conditions are determined dynamically at every grid point by solving the SEB. See Appendix A for other numerical details of the code.

The SEB for an infinitesimally thin layer at the ground surface can be written (following Brutsaert, 1982; Chang et al., 1999):

$$R_n = H + LE + G + Misc \tag{1}$$

where radiation fluxes toward the surface are taken as positive and all other fluxes are considered positive when leaving the surface. This sign convention is loosely based on the premise that radiation drives the energy of the surface and that the other energy fluxes are the means by which the surface disposes of the absorbed radiation. In Equation (1), R_n is the net radiation, which can be broken down into the sum of its parts: $R_n = R_s(1-\alpha) + \epsilon R_{dn} - \epsilon\sigma T_s^4$, where R_s is the incoming solar radiation, α is the albedo of the surface, ϵ is the surface emissivity, R_{dn} is the downwelling long-wave radiation, σ is the Stefan-Boltzman constant, and T_s is the surface temperature. H is the sensible heat flux, parameterized as $-\rho C_p C_h U(\theta_a - \theta_s)$ where ρ is the air density, C_p is the specific heat of the air, C_h is an exchange coefficient for heat, U is the wind speed immediately above the surface, and θ_a and θ_s are the potential temperature of the air and ground surface respectively. LE is the latent heat flux, parameterized as $-\rho L C_e U(q_a - q_s)$ where L is the latent heat of vaporization, C_e is an exchange coefficient for vapor, and q_a and q_s are water vapor mixing ratio of the air and ground surface respectively. G is the soil heat flux which can be parameterized

as $k_T(\Theta_1)\frac{T_s-T_1}{z_1}$, where $k_T(\Theta_1)$ is the soil thermal conductivity that depends on the soil moisture Θ_1 at the first soil level z_1 and soil type. *Misc.* represents other terms such as contributions from precipitation, melting snow, horizontal advection, or storage, which we ignore. Dynamically, the atmosphere and land-surface are coupled through the surface momentum flux. The surface momentum flux is parameterized as $\tau = \rho u_*^2 = \rho C_m U^2$, where u_* is the friction velocity and C_m is the drag coefficient. Through dynamic calculation of τ, R_n, H, LE, and G the atmosphere is therefore directly coupled to the land-surface.

This coupling is also a natural mechanism to undertake an investigation into the influence of land-surface heterogeneity on PBL structure. It is known that under free convective (no wind) conditions, imposed land-surface heterogeneity induces organized atmospheric motions (*e.g.,* Hadfield et al., 1991), but how these organized motions feed back to dry/cool the soil, and how that drying/cooling influences the organized motions has yet to be established. In the horizontal, landscape heterogeneity has been shown to influence the PBL structure at scales up to 40 km (Avissar and Schmidt, 1998). However, the typical (x,y,z) domain of LES studies of the PBL to date is about $5 \times 5 \times 2$ km^3 (*e.g.,* Moeng, 1984; Hadfield et al., 1991). Therefore, in order to incorporate heterogeneous land-surface forcing in our simulations, it is imperative that we consider computational domains and time-scales that are large compared to those routinely considered in LES of the PBL. Therefore, an LES that utilizes adequate resolution to capture turbulence and at the same time covers a large horizontal domain requires large numbers of grid points. For example, in a $30 \times 5 \times 3$ km^3 domain, 9×10^6 grid points are required for a mesh size of $50 \times 50 \times 20$ m^3.

3. The LSM: Deployment, Input Parameters, and Initial Conditions

The LSM is implemented at every (x,y) grid point in the LES. Each of these grid points is covered by perennial grasses, with a roughness length for momentum z_{o_m} of 0.1 m, and overlays four silty clay loam soil layers at depths of [0.05, 0.20, 0.60, 1.00] m. Since the surface is covered by grasses, we assume a constant surface albedo of 0.2 across the domain for all cases. All snow and ice components of the LSM are turned off. The exchange coefficients for momentum, heat, and moisture (C_m, C_h, C_e) are evaluated locally at every timestep based on Paulson's (1970) similarity functions. C_h and C_e are assumed equal.

In the LSM, the parameter c_z defines the relationship between the roughness height for momentum z_{o_m} and the roughness height for heat z_{o_h}:

$$z_{o_h} = z_{o_m}\, e^{-(258\, c_z\, \kappa\, u_*\, z_{o_m})}. \tag{2}$$

To determine the value of c_z, following Brutsaert (1982) we assume that the exchange coefficients for momentum (C_m) and heat (C_h) are related by the expression: $C_m/C_h \sim 3$, which is valid for bluff bodies (see Figure 5.4, Brutsaert, 1982). Assuming the drag law to be applicable, we know that $C_m = u_*^2/U^2$ and $C_h = \theta_*/(\Delta\theta\, U)$. Therefore $C_m/C_h = ln(z_{o_m}/z_{o_h})$, or $z_{o_m}/z_{o_h} = e^3$. Substituting into Equation (2) gives $c_z = 0.1$. This is different from the default value (c_z=0.2) in NOAH thereby increasing the efficiency of surface scalar exchange compared to NOAH's default, but is derived directly from an understanding of land-surface

exchange at the scale of interest.

In addition to modifying c_z, the LSM needed another modification to be applicable for the relatively small-scale application discussed here. As it was obtained from the National Centers for Environmental Prediction (NCEP), the LSM assumes the convective scaling velocity $[w_* = \langle \frac{g}{\rho}\, z_i\, (\frac{H}{\theta_\circ C_p} + 0.61E) \rangle^{1/3}]$ is the minimum wind speed to avoid singular solutions under zero wind (free convection) conditions. While this assumption may be reasonable for the larger-scale flows where the PBL is not resolved, w_* is a bulk PBL parameter and would therefore decouple the soil from the local overlying atmosphere. To remain consistent with our adopted coupling method (through drag law assumptions), we assume a local drag law formulation to determine a small convective velocity scale following Schmidt and Schumann (1989) such that the minimum wind speed at the ground surface is dynamically calculated from the following:

$$u_{min} = 0.07(\frac{g}{\theta_\circ}\, \Delta z\, C_h\, \Delta\theta_v)^{\frac{1}{3}} \tag{3}$$

where, g is the gravitational acceleration, $\theta_\circ$ is a reference temperature, Δz is the distance between the ground and the first grid point above the surface, C_h is the exchange coefficient for heat derived by the LSM and $\Delta\theta_v$ is the virtual potential temperature gradient between the same two heights.

[Figure 1 about here.]

Initial soil conditions were taken from ground-based measurements at the Little Washita

site on Day 193 of the Southern Great Plains 1997 (SGP97) experiment. This day and location were chosen because nearly an inch of rain fell on the preceding 1.5 days and they coincided with an intensive observing period. The observations were interpolated to the four soil levels in the LSM. Before using these as initial conditions for the LES-LSM runs, the soil model was run off-line for four complete diurnal cycles to allow the LSM to equilibrate. The noon-time conditions after these four diurnal cycles were used as the *wet* initial soil conditions (Figure 1). It is important to note that these *wet* initial soil conditions are such that the evaporation will be determined by a combination of the available soil moisture and the atmospheric demand rather than at the evaporative potential rate. *Dry* soil conditions were obtained by running the off-line LSM further for another seven diurnal cycles allowing the soil to dry under realistic forcing. Noon-time conditions after the seven day dry down period were chosen as *dry* conditions (Figure 1). *Average* initial soil conditions were obtained by picking the noon-time soil conditions that provided surface fluxes nearly equal to the noon-time fluxes averaged every day over the entire one-week dry-down period.

4. Simulations

The coupled LES-LSM simulations employ (600,100,144) grid points in the (x,y,z) directions representing a (30,5,2.88) km domain. This leads to a grid spacing of (50,50,20) meters in each of the (x,y,z) directions.

A geostrophic wind of 0 m s^{-1} is imposed in both x and y directions, therefore the simulations are in the free convection limit. The only external forcing imposed on the

system is specified through the incoming solar radiation, which is set to 700 W m^{-2} and is constant in time for all cases.

For all of the simulations, the initial potential temperature is constant with height (300K) below 790m. A capping inversion is imposed (3K/0.1km) between 790 m and 890 m, and the middle of this layer we call the initial inversion height, z_i = 840 m; above 890 m the stratification is 3 K/km (Figure 2).

[Figure 2 about here.]

Two different PBLs are simulated with varying moisture content. In the first set of cases, the PBL was initialized dry (1 g kg^{-1}) throughout the entire domain (DP, dry PBL). The second set of cases was initialized with a relatively wet atmosphere (8 g kg^{-1}) in the PBL, dropping sharply to 1 g kg^{-1} across the initial inversion layer, between 790 and 840 m (WP, wet PBL). See Figure 2 for a visual representation of the initial DP and WP conditions.

For each of the DP and WP cases, nine simulations were performed. Three of these are horizontally homogeneous cases with uniform soil conditions that are *wet* (WS), *dry* (DS), and *average* (AS) respectively. The subsequent six cases are initialized with horizontally heterogeneous soil conditions. The heterogeneity that is imposed occurs solely in the x-direction as a step-function change between *wet* and *dry* soil. We define λ as the wavelength of one complete *wet* and *dry* cycle. The wavelengths vary as λ = [2, 3, 5, 7.5, 15, 30] km. At initial times, the x-extent of a single patch ($\lambda/2$) ranges therefore from $1.2z_i$ to $17.8z_i$. The soil conditions are homogeneous in the y-direction for all simulations.

The nomenclature used to discuss the cases from here on will adhere the following format:

The case name includes a description of the initial PBL moisture content followed by a description of the underlying soil conditions (separated by a hyphen). For example, case DP-WS refers to the run which was initiated with a *dry* PBL and a horizontally homogeneous *wet* soil condition, and case WP-7.5S refers to the case initialized with a *wet* PBL and a λ = 7.5 km wavelength heterogeneous soil condition. The rest of the names follow accordingly (see Table 1).

Each simulation is integrated out in time until the turbulence is in equilibrium with its external forcing. This time is defined by the necessary time for the boundary layer averaged turbulence kinetic energy and the boundary layer growth rate to become nearly constant. These criteria were typically satisfied within (2.8-3.3, 1.9-2.5) hours for the (DP, WP) cases, respectively. The time steps for these simulations were variable but ranged between (0.7-1.6, 1.4-1.7) s. Therefore, the simulations were integrated for about (6000, 4000) time steps before any averaging began. Statistics were calculated over the subsequent 4000 time steps, or about (4-9, 8-10) turnover times, where a turnover time t_* is defined as z_i/w_*. For normalization purposes, we define $\theta_* = H/(\rho C_p w_*)$, $\Theta_* = E/(\rho w_*)$ and $\theta_{v*} = (\frac{H}{C_p} + 0.61\,\theta_\circ\,E)/(\rho w_*)$. See Table 1 for the horizontally- and time-averaged values of these quantities.

[Table 1 about here.]

5. Verification

As mentioned above, large numbers of grid points are required to investigate desired scale range of heterogeneity while maintaining the ability to resolve the response of important

PBL scales of motion. Therefore, before performing the land-surface coupling, the NCAR LES code was ported from a shared memory (Cray vector supercomputer) environment to a distributed memory massively parallel (*e.g.,* IBM SP3 supercomputer) environment using the Message Passing Interface (MPI). A single MPI decomposition in the vertical direction is used, which is natural since finite differences are employed in the vertical direction and a spectral representation in the horizontal directions. Initial tests of the new code indicate that the code scales well, *i.e.,* the wall clock time decreases linearly as the number of MPI processes increases (not shown). Each simulation discussed in this manuscript took about (54,45) wall clock hours for the (DP, WP) cases on 48 IBM SP3 CPUs, or about (2592, 2160) CPU hours. In order to achieve acceptable efficiency in the coupled LES-LSM, it was also necessary to parallelize the LSM portion of the code across all MPI tasks.

5.1 Comparison to Previous Studies

Before embarking towards an extensive study with the newly developed coupled LES-LSM, tests were performed to verify that results generated were comparable to previous research. The investigation presented by Schmidt and Schumann (1989) is considered the first to examine the free convective PBL in a robust and concise manner. The same case as Schmidt and Schumann (1989) was run with the new code. The main difference between the simulations is that the current simulation uses a coupled land-surface boundary condition. Through 1-D off-line LSM testing we devised a set of soil conditions and incoming solar radiation that would provide surface fluxes similar to those imposed in Schmidt and Schumann (1989).

Measurements from the Willis and Deardorff (1974) tank experiments provide observational support.

[Figure 3 about here.]

The variances and SGS energy from the coupled code are slightly larger in magnitude through the majority of the PBL than those of Schmidt and Schumann (1989) (Figure 3), which is consistent with the comparison of these codes presented in Nieuwstadt et al. (1993). Notable, however, is that the current coupled code outperforms Schmidt and Schumann (1989) code at reproducing the turbulent statistics from the Willis and Deardorff (1974) tank experiments. These results provide confidence that incorporating the LSM at the lower boundary and porting the code to massively parallel machines has not dramatically altered the performance of the code.

5.2 Evaluation of lateral domain size

The imposed heterogeneity varies only in the x-direction, not in y. Therefore, we utilize a large domain in the x-direction and a relatively small domain in the y-direction. It is prudent to evaluate whether the relatively short lateral extent of the domain influences the flow that ensues. If the y-domain is too small, the organized motions that develop will become artificially coupled through the periodic boundary conditions. To evaluate whether our domain choice is large enough to represent that of an infinite domain, two additional simulations were performed. These cases are identical to case DP-15S except that the y-domain is either halved or doubled. Therefore, the two cases utilize 50 or 200 nodes to

represent 2.5 or 10 km in y, respectively. We chose to evaluate the DP-15S case since the heterogeneity strongly influenced the statistics (to be shown in Section 6.).

[Figure 4 about here.]

Following the analysis of Komminaho et al. (1996), too small a domain should reveal itself through amplification of two-point horizontal velocity correlations $[R_{uu}(\Delta y)]$ with increasing lag in the lateral direction (Δy). Comparison of R_{uu} (Figure 4a) suggests that halving the domain size amplifies the lateral correlation of horizontal velocity (most noticeable at $\Delta y = 1.2$ km). Doubling the size of the lateral dimension has some impact on the correlations, slightly increasing the amplitude at $\Delta y = 1.2$ km and minimally decreasing the lateral distance corresponding to the first zero-crossing. Vertical profiles of normalized horizontal root-mean-square velocities (u_{rms}/w_*, where $u_{rms} = \langle u''^2 + \frac{2}{3}e \rangle^{1/2}$) confirm that the extent of the lateral domain has little influence on predicted turbulence statistics (Figure 4b). Therefore, through this analysis we are reasonably confident that our domain choice of $30 \times 5 \times 2.88$ km^3 does not adversely influence the quantitative results and adequately represents simulations of heterogeneity that infinitely span the lateral dimension.

6. Results

6.1 Instantaneous Fields

6.1.1 Horizontally Varying Land-Surface Properties and Forcing

[Figure 5 about here.]

As an example, instantaneous horizontal slices of land surface properties from the last time step of simulation DP-AS (Figure 5) show evidence of the coupling between the PBL and the underlying soil. The surface heat fluxes (sensible, latent and soil) contain the signature of cellular convection suggesting that the exchange at the ground surface is driven by atmospheric demand. Also notice that the soil temperature and moisture at the first model level in the LSM provide evidence of spatially varied drying and warming; at this last time step, the soil has dried considerably since initialization as it began with a horizontally homogeneous distribution of 21.5% volumetric soil moisture. The soil temperature at the first model level has also increased from its initial horizontally homogeneous value of about 309 K. Cases with heterogeneity reveal a similar evolution and pattern but those patterns are dominated by the disparity between *wet* and *dry* soil. Patton et al. (2003b) presents results and discussion of the surface fluxes as influenced by the heterogeneity-induced organized motions.

6.1.2 The PBL

[Figure 6 about here.]

[Figure 7 about here.]

For the DP cases, the influence of the varying soil moisture is evident in the flow visualization of vertical velocity and water vapor mixing ratio contours shown in Figures 6 and 7. These figures show how the presence or absence of soil moisture variation dramatically alters the turbulent motions in the PBL. Over the region of high soil moisture content (*e.g.*,

x = [0,3.75], [7.5,11.25], [15,18.75], [22.5,26.25] km, Figure 7) the convective plumes tend to be less vigorous compared to their counterparts in the region of low soil moisture content.

At the same time, the shape of the PBL interface layer (*i.e.,* the entrainment zone around z = 1.3 to 1.5 km) is also altered by soil moisture heterogeneity. Entrainment of low water vapor mixing ratio is observed over the region of high soil moisture and entrained dry air extends all the way to the ground (compare the second panels of Figures 6 and 7) In general, we see evidence of entrainment of dry air near the plume valleys, similar to that reported by Sullivan et al. (1998). The average normalized mixing ratio in the domain is about the same for the two cases (not shown), but in the DP-7.5S case, averaged vertically, the lowest PBL mixing ratio exists over the soil with the highest volumetric soil moisture; results presented in Patton et al. (2003b) will quantify the organized motions responsible for these patterns.

The bottom two panels of Figures 6 and 7 show the x-variation of the associated instantaneous surface fluxes and volumetric soil moisture at the uppermost LSM level. In contrast to studies with specified surface fluxes, the fluxes in the current simulations are spatially varying and respond to both the PBL and to soil temperature/moisture. The partitioning of energy by the LSM is evident in both figures, but especially in Figure 7 where over the *wet* soil a greater portion of the available energy goes into evaporating water and hence larger latent and smaller sensible heat fluxes compared to that over *dry* soil. Figures 6 and 7 are presented as examples; the picture is similar for the other heterogeneous cases.

6.2 Bulk Boundary Layer Statistics

6.2.1 Surface Fluxes

Since the only external input of energy to the simulations is the specified incoming solar radiation, the surface buoyancy forcing θ_{v*} is dynamically determined through the LES-LSM coupling. Therefore, it is prudent to quantify the bulk forcing on the PBL. To do so, the horizontally- and time-averaged sensible heat flux (H), latent heat flux (LE) and the Bowen ratio ($\beta = H/LE$) are calculated. These quantities are presented in Table 1. Note that θ_* and Θ_* can be calculated from H and LE, and can be combined into θ_{v*}, the surface virtual temperature flux using $\theta_{v*} = \theta_* + (0.61\,\theta_o\,\Theta_*)$, where θ_o is a reference potential temperature. θ_{v*} is used throughout the manuscript as the scaling parameter for virtual potential temperature. Table 1 also includes the horizontally- and time-averaged boundary layer heights (z_i) and the convective velocity (w_*). Here, z_i is determined by finding the local height of the largest gradient in virtual potential temperature profile at every (x, y) location and averaging across all x and y. This method to determine z_i was first described as the gradient method in Sullivan et al. (1998), and further described as a wavelet method of minimum dilation in Davis et al. (2000).

As expected, the horizontally homogeneous *dry* soil cases (DS) partition 7.5-7.7 times more incoming solar radiation into sensible heat compared to latent heat than does the *wet* soil case (WS). Also apparent from Table 1 is that our attempt to pick soil conditions for the *average* (AS) cases that resulted in average surface fluxes equal to the average of the WS and DS cases was not completely successful, *e.g.*, θ_{v*} of the AS cases is larger than the

average of those of WS and DS. Nonetheless, we can still use these AS cases as a point of reference. Scaling parameters z_i and w_* reveal the expected influence of the magnitude of the surface buoyancy forcing θ_{v*}; the larger θ_{v*}, the larger are z_i and w_*. Worth noting is that the land-surface model responds as expected to the moisture-state of the PBL; when the PBL is of higher average mixing ratio there is less atmospheric demand for moisture at the ground which is reflected in lower evaporative fluxes in the WP cases compared to the DP cases.

6.2.2 Surface Exchange Coefficients

[Figure 8 about here.]

As mentioned earlier, at every (x,y) location in the domain the surface fluxes of momentum, heat and moisture in these simulations are internally determined through a coupling between a partitioning of the available energy energy via the SEB and a drag law. The efficiency of the transfer between the land-surface and the PBL is determined by drag coefficients (C_m, C_h) which are dynamically calculated from surface similarity theory assumed valid locally between the ground and the first LES grid level (which due to the staggered vertical grid system in the LES is 10 m for the u,v-velocities). Again, we assume that the exchange coefficient for moisture is the same as that for heat.

On average, small-scale land-surface heterogeneity ($\lambda/z_i \sim$ 1-2) increases the exchange coefficients for momentum and heat (Figure 8), while larger-scale heterogeneity ($\lambda/z_i \sim$ 4-9) tends to reduce these exchange coefficients. For flows encountering even larger-scale

heterogeneity ($\lambda/z_i \sim 17$), the coefficients decrease compared to $\lambda/z_i \sim$ 4-9 heterogeneity and are tending back toward the values determined from the homogeneous cases. C_m and C_h for the $\lambda/z_i \sim$ 4-9 cases are about 6% and 9% lower compared to the AS cases. It is understood that C_m and C_h are wind speed dependent (Schlichting, 1979; Brutsaert, 1982; Mahrt et al., 2001b), and that they decrease with increasing wind speed. The organized motions that develop as a result of the heterogeneity (see Patton et al., 2003b), are most intense for the $\lambda/z_i \sim$ 4-9 cases. Therefore, the decrease in C_m and C_h for these cases likely results from a persistent increase in surface winds associated with the organized motions.

Comparing the left and right panels of Figure 8, there is little or no influence of the initial PBL water vapor mixing ratio on the efficiency of the surface exchange which is consistent with Schlichting's (1979) dimensional analysis suggesting that C_m should only be a function of Reynold's number[†]. While the $\lambda/z_i \sim$ 4-9 cases show the smallest C_m and C_h, their surface fluxes of heat and moisture are larger than the others (Table 1). This indicates that the gradients of heat and moisture between the ground surface and the first model level are larger on average for these cases than for the other heterogeneous soil cases. This increased gradient manifests itself through slightly lower average soil temperatures and volumetric moisture content combined with slightly higher PBL temperatures and water vapor mixing ratios (not shown). Although the effects are relatively small, this analysis implies greater transfer of heat and moisture from the soil to the PBL in the presence of $\lambda/z_i \sim$ 4-9 scale heterogeneity.

[†]Note that C_h depends on C_m (Brutsaert, 1982).

6.2.3 Turbulence Kinetic Energy

[Figure 9 about here.]

Total turbulence kinetic energy (averaged over the PBL and time, $\langle\ \rangle_{PBL,t}$) responds to land-surface heterogeneity (Figure 9). Heterogeneity at scales larger than 3 km increases the volume- and time-averaged turbulent kinetic energy. The increase in turbulence kinetic energy is due to the generation of organized motions (discussed in Patton et al., 2003b). Hadfield et al. (1991) also discussed circulations such as these in their LES simulations, but suggested that the circulation is weak since it only accounts for $\approx$1% of the kinetic energy in the PBL. The Hadfield et al. (1991) study, however, only looked at two wavelengths of heterogeneity, λ = (1.5, 4.5) km, both of which fall at the small-scale end of this study and are in agreement with these results. As the scale of the heterogeneity increases towards a wavelength of 15 km, the circulation becomes stronger, and then decreases again at even larger scales. The TKE is most affected for cases DP-15S and WP-15S ($\lambda/z_i \sim 9$) which reveal an increase of (14, 19)% respectively compared to the horizontally homogeneous cases.

6.2.4 PBL Height and Entrainment Rates

[Figure 10 about here.]

The growth of the convective layer is tied to the mixing process that occurs at the density interface between the well mixed PBL and the non-turbulent overlying stable layer (Sullivan et al., 1998). Apparent from Figures 6 and 7, under free convection, heterogeneous soil

moisture induces organized PBL motions that alter how the PBL operates. Therefore, it is anticipated that heterogeneity could modify the growth rate of the PBL.

Figure 10 depicts the time evolution of the horizontally averaged boundary layer height for all cases. The times presented represent the entire averaging period for our statistics representing (4-9, 8-10) large eddy turnover times (z_i/w_*) for the (DP, WP) cases, respectively. The average boundary layer growth is linear with time suggesting that the flow is quasi-steady. All heterogeneous cases fall between the horizontally homogeneous extreme cases (DS and WS).

[Figure 11 about here.]

Entrainment rates ($w_e = \partial z_i/\partial t$) are calculated by performing a least-squares fit to the data presented in Figure 10, taking the slope of the fitted line to be w_e. Heterogeneity and the initial PBL moisture only slightly modify the normalized entrainment rates (Figure 11). Heterogeneity-scales on the order of the PBL depth tend to decrease normalized entrainment rates compared to the AS cases, although this decrease is only (5.6, 5.5)% for the (DP, WP) cases respectively. Heterogeneity-scales of (9, 5) times z_i slightly increase the entrainment rates for the (DP, WP) cases, but this increase is only (5.3, 3.8)% compared to the AS cases, respectively. These entrainment rates are also slightly higher than the homogeneous dry soil cases (DS). Even larger heterogeneity ($\lambda/z_i \sim 18$) tends to slightly decrease entrainment rates. These results are counter to Avissar and Schmidt's (1998) comments that heterogeneously-induced organized motions dramatically increase the rate at which the PBL entrains. However, they made these comments without actually calculating w_e/w_*. Simi-

lar rates of entrainment are found for the homogeneous cases when comparing dry versus wet PBLs (compare the left and right panels of Figure 11). For both homogeneously- and heterogeneously-forced PBLs, the normalized entrainment rates presented in Figure 11 are noticeably higher (~ 0.04) than those presented in Sullivan et al. (1998) (~ 0.02) due to both the relatively weak inversion and to the strong surface forcing in these simulations compared to those in Sullivan et al. (1998).

The combined results presented in Figures 9 and 11 indicates that the entrainment rate is not directly proportional to TKE, rather entrainment appears more dependent on the rate of heating. We can only make this statement as it applies to free convective PBLs interacting with and in equilibrium with strip-like heterogeneity.

6.3 Horizontally Averaged Statistics

6.3.1 Velocity Variances

[Figure 12 about here.]

[Figure 13 about here.]

The moisture state of the PBL does not vastly influence horizontal and vertical velocity variances (Figures 12 and 13). Compared to the horizontally homogeneous cases, $\langle u''^2 \rangle / w_*^2$ near the ground and entrainment zone follows a natural progression (increase, peak, and decrease) when transitioning from small-scale (2 km, $\lambda / z_i \sim 1$) to large-scale (30 km, $\lambda / z_i \sim 18$) heterogeneity (Figure 12). Lateral variances ($\langle v''^2 \rangle / w_*^2$) are quite similar for all cases (not shown).

The increase in horizontal velocity fluctuations, at both the ground and z_i, is consistent with the presence of 2-D organized circulations induced by the strip-like heterogeneity. Hadfield et al. (1991) and Avissar and Schmidt (1998) both showed velocity fluctuations to increase at these locations in the presence of heterogeneity. However, Hadfield et al.'s (1991) largest heterogeneity scale (λ/z_i) was about 4 and they were therefore unable to trace the pattern back towards homogeneity with increasing λ/z_i as depicted in Figure 12. Avissar and Schmidt's (1998) results, however, suggested that for this surface heat flux across the patches (~ 0.1 m K s^{-1}) the fluctuations should trace the pattern like that in Figure 12.

With the exception of the increase of $\langle u''^2 \rangle / w_*^2$ near z_i, the response of the velocity variances to heterogeneity (Figures 12 and 13) is strikingly similar to the expected change between shear- and buoyancy-driven PBLs. Moeng and Sullivan (1994) showed $\langle u''^2 \rangle / w_*^2$ to increase appreciably near the ground in the presence of a mean velocity shear. They also showed $\langle w''^2 \rangle / w_*^2$ to decrease in the mid-PBL for increasing shear. Therefore at least with respect to velocity variances, these free convective PBLs in the presence of land-surface heterogeneity are somewhat analogous to free convective PBLs over homogeneous surfaces but with a mixed shear-buoyant forcing.

6.3.2 Vertical Scalar Flux

[Figure 14 about here.]

For the DP PBLs, profiles of normalized vertical mixing ratio flux show only a small influence of surface heterogeneity (left panel, Figure 14). WP cases also show little influence

of heterogeneity (right panel, Figure 14), but the horizontally homogeneous cases reveal the influence of the soil partitioning of the available solar energy. As discussed in Section 6.2.1, case WP-DS partitions less available energy into latent heat and therefore more energy goes into sensible heat. Case WP-DS also entrains nearly three times more dry air than does WP-AS due to the much larger moisture jump across z_i.

[Figure 15 about here.]

Normalized profiles of vertical virtual potential temperature flux are linear through the PBL suggesting that our averaging is sufficient to assume quasi-steady conditions (Figure 15). These results are counter to earlier findings (Avissar and Schmidt, 1998) who suggested that vertical potential temperature flux profiles are dramatically modified by heterogeneity. The profiles reveal very little modification due to land-surface heterogeneity no matter if the PBL is initially dry or wet (Figure 15). These results are consistent with the entrainment rate calculations presented in Figure 11, and suggest that the moisture component is truly not passive. In all cases, the profiles have a minimum flux (just below z_i) to surface flux ratio of about -0.12 which is smaller than the traditional value of -0.2 (Deardorff, 1979). According to Lilly (2002), this smaller minimum flux to surface flux ratio results from horizontal averaging across an undulating interface.

7. Summary and Conclusions

We have developed a large-eddy simulation code coupled with a fully interactive land-surface model. Initial temperature and moisture conditions are specified for the PBL and the soil

and are taken from SGP97 measurements. No mean wind is imposed such that the incoming solar radiation is the only external forcing in the simulations. The results show that soil moisture content is a crucial variable influencing PBL motions.

Visualizations of instantaneous fields reveal the signature of cellular convection at the surface and in the soil. Instantaneous slices of the PBL show dramatic modification of the PBL structure resulting from soil moisture heterogeneity. Instantaneous surface fluxes also depict the dynamic response of the forcing to the PBL.

Consistent with previous research, under free convective conditions, heterogeneity generates organized motions. Heterogeneity at scales ranging from $\lambda/z_i \sim$ 4-9 induces the greatest PBL response. The organized motions induced at these scales of heterogeneity decrease the exchange coefficients for (momentum, scalars) by about (6, 9)% compared to the homogeneous average soil cases (AS), and increase the bulk turbulence kinetic energy of the PBL by about 20%. The generation of these organized motions and the subsequent increase in turbulence kinetic energy, however, do not dramatically influence entrainment rates.

Implications from these findings are that large-scale models that cannot resolve land-surface heterogeneity will slightly underestimate the surface fluxes of heat and moisture, but should not mis-estimate PBL entrainment. With respect to surface-layer turbulence statistics, heterogeneity makes the buoyantly forced PBLs appear more like mixed shear-buoyancy PBLs due to the induced organized motions.

Acknowledgements:

NCAR is sponsored by the National Science Foundation. This work was supported in part by the NASA Land Surface Hydrology program through contract NAG5-8839. We thank Michael Ek from NCEP for supplying us with the NOAH land surface model and for helpful discussions, and Don Lenschow and Peggy Lemone for comments on an earlier version of this manuscript.

Appendix A: Numerics

For all variables the LES uses pseudo-spectral differencing in the horizontal. For velocities, the LES uses second-order centered-in-space differencing, while for scalars the monotone advection scheme of Koren (1993) is used. Spalart et al.'s (1991) third-order Runge-Kutta scheme advances all fields in time using a fixed Courant-Friedrichs-Lewy (CFL) number of 0.63 for a complete 3-stage time step. Periodic boundary conditions are imposed in the horizontal. To allow the propagation of gravity waves out of the top of the domain, the upper boundary condition is that of Klemp and Durran (1983). Because the LES uses spectral differencing in the horizontal, the MPI implementation breaks up the domain in the vertical into slabs of horizontal data residing on a single processor. To perform the spectral decomposition, we use NCAR's FFTPACK version 4.1 (http://www.scd.ucar.edu/softlib/FFTPACK.html).

In the LSM, upwind finite differences are used for vertical derivatives and the Crank-Nicholson scheme is used for time differencing. At the lower boundary, the hydraulic diffusivity is assumed to be zero so that the soil water flux is is determined solely by gravitational

conduction. The soil heat flux is computed from a vertical temperature gradient between the lowest LSM model level and a specified soil temperature at an imaginary grid point one meter below the bottom of the model. Further details can be found in Mahrt and Pan (1984), Pan and Mahrt (1987), and Chang et al. (1999). To improve scalability when solving the LSM for the coupled surface boundary condition, we use MPI to break up the calculation in the x-direction.

References

Albertson, J. D., W. P. Kustas, and T. M. Scanlon, 2001: 'Large-eddy simulation over heterogeneous terrain with remotely sensed land surface conditions', *Water Resour. Res.*, **37, 7**, 1939–1953.

Albertson, J. D. and M. B. Parlange, 1999: 'Natural integration of scalar fluxes from complex terrain', *Adv. Water Resourc.*, **23**, 239–252.

Avissar, R. and T. Schmidt, 1998: 'An evaluation of the scale at which ground-surface heat flux patchiness affects the convective boundary layer using large-eddy simulations', *J. Atmos. Sci.*, **55**, 2666–2689.

Brutsaert, W., 1982: *Evaporation into the Atmosphere*, Kluwer Academic Publishers, Dordrecht, The Netherlands, 299pp pp.

Chang, S., D. Hahn, C.-H. Yang, and D. Norquist, 1999: 'Validation of the CAPS model land surface scheme using the 1987 Cabauw/PILPS dataset', *J. Appl. Meteorol.*, **38**, 405–422.

Davis, K. J., N. Gamage, C. R. Hagelberg, C. Kiemle, D. H. Lenschow, and P. P. Sullivan, 2000: 'An objective method for deriving atmospheric structure from airborne LIDAR observations', *J. Atmos. Oceanic Tech.*, **17**, 1455–1468.

Deardorff, J. W., 1979: 'Prediction of convective mixed-layer entrainment for realistic cpping inversion structure', *J. Atmos. Sci.*, **36**, 424–436.

Esau, I. N. and T. J. Lyons, 2002: 'Effect of sharp vegetation boundary on the convective atmospheric boundary layer', *Agric. For. Meteorol.*, **114**, 3–13.

Garratt, J. R., 1993: 'Sensitivity of climate simulations to land-surface and atmospheric boundary-layer treatments - A review', *J. Clim.*, **6**, 419–448.

Hadfield, M. G., W. R. Cotton, and R. A. Pielke, 1991: 'Large-eddy simulations of thermally forced circulation in the convective boundary layer. Part I: A small scale circulation with zero wind', *Boundary-Layer Meteorol.*, **57**, 79–114.

Hechtel, L. M., C.-H. Moeng, and R. B. Stull, 1990: 'The effects of nonhomogeneous surface fluxes on the convective boundary layer: A case study using large-eddy simulation', *J. Atmos. Sci.*, **47**, 1721–1741.

Klemp, J. B. and D. R. Durran, 1983: 'An upper boundary condition permitting internal gravity wave radiation in numerical mesoscale models', *Mon. Wea. Rev.*, **111**, 430–444.

Komminaho, J., A. Lundbladh, and A. V. Johansson, 1996: 'Very large structures in plane turbulent Couette flow', *J. Fluid Mech.*, **320**, 259–285.

Koren, B., 1993: 'A robust upwind discretization method for advection, diffusion and source terms', in *Numerical Methods for Advection-Diffusion Problems*, edited by C. B. Vreng-denhil and B. Koren, volume 45 of *Notes on Numerical Fluid Mechanics*, chapter 5, pp. 117–138, Vieweg Verlag, Braunschweig, Germany.

Kustas, W. P. and J. D. Albertson, 2003: 'Effects of surface temperature contrast on land-atmosphere exchange: A case study from Monsoon 90', *Water Resour. Res.*, **39, 6**, 1159–1174.

Lilly, D. K., 2002: 'Entrainment into mixed layers. Part I: Sharp-edged and smoothed tops', *J. Atmos. Sci.*, **59**, 3340–3352.

Mahrt, L. and H. Pan, 1984: 'A two-layer model of soil hydrology', *Boundary-Layer Meteorol.*, **29**, 1–20.

Mahrt, L., D. Vickers, and J. Sun, 2001a: 'Spatial variations of surface moisture flux from aircraft data', *Adv. Water Resourc.*, **24**, 1133–1141.

Mahrt, L., D. Vickers, J. Sun, N. O. Jensen, H. Jørgensen, E. Pardyjak, and H. Fernando, 2001b: 'Determination of the surface drag coefficient', *Boundary-Layer Meteorol.*, **99**, 249–276.

McNaughton, K. G. and M. R. Raupach, 1996: 'Responses of the convective boundary layer and the surface energy balance to large-scale heterogeneity', in *Scaling up in Hydrology using Remote Sensing*, edited by J. B. Stewart, E. T. Engman, R. A. Feddes, and Y. Kerr, pp. 171–182, John Wiley & Sons, Chichester.

Moeng, C.-H., 1984: 'A large-eddy simulation model for the study of planetary boundary-layer turbulence', *J. Atmos. Sci.*, **41**, 2052–2062.

Moeng, C.-H. and P. P. Sullivan, 1994: 'A comparison of shear- and buoyancy-driven planetary boundary layer flows', *J. Atmos. Sci.*, **51**, 999–1022.

Nieuwstadt, F. T. M., P. J. Mason, C.-H. Moeng, and U. Schumann, 1993: 'Large-eddy simulation of the convective boundary layer: A comparison of four computer codes', in *Turbulent Shear Flows 8*, edited by F. Durst, R. Friedrich, B. E. Launder, F. W. Schmidt, U. Schumann, and J. H. Whitelaw, Springer–Verlag, Berlin.

Pan, H.-L. and L. Mahrt, 1987: 'Interaction between soil hydrology and boundary layer development', *Boundary-Layer Meteorol.*, **38**, 185–202.

Patton, E. G., P. P. Sullivan, and C.-H. Moeng, 2003b: 'Influence of idealized heterogeneity on wet and dry planetary boundary layers coupled to the land surface; II: Phase-averaged fields', *J. Atmos. Sci.*, **Submitted**.

Paulson, C. A., 1970: 'The mathematical representation of wind speed and temperature profiles in the unstable atmospheric surface layer', *J. Appl. Meteorol.*, **9**, 857–861.

Raasch, S. and G. Harbusch, 2001: 'An analysis of secondary circulations and their effects caused by small-scale surface heterogeneities using large-eddy simulation', *Boundary-Layer Meteorol.*, **101**, 31–59.

Raupach, M. R., 2000: 'Equilibrium evaporation and the convective boundary layer', *Boundary-Layer Meteorol.*, **96**, 107–141.

Rowntree, P. R. and J. Bolton, 1983: 'Simulation of the atmospheric response to soil moisture anomalies over Europe', *Quart. J. Roy. Meteorol. Soc.*, **109**, 501–526.

Schlichting, H., 1979: *Boundary-Layer Theory*, McGraw-Hill, Inc., New York, 817 pp.

Schmidt, H. and U. Schumann, 1989: 'Coherent structure of the convective boundary layer derived from large-eddy simulation', *J. Fluid Mech.*, **200**, 511–562.

Shen, S. and M. Y. Leclerc, 1995: 'How large must surface inhomogeneities be before they influence the convective boundary layer structure? A case study', *Quart. J. Roy. Meteorol. Soc.*, **121**, 1209–1228.

Spalart, P. R., R. D. Moser, and M. M. Rogers, 1991: 'Spectral methods for the Navier-Stokes equations with one infinite and two periodic directions', *J. Comp. Phys.*, **97**, 297–324.

Sullivan, P. P., J. C. McWilliams, and C.-H. Moeng, 1996: 'A grid nesting method for large-eddy simulation of planetary boundary-layer flows', *Boundary-Layer Meteorol.*, **80**, 167–202.

Sullivan, P. P., C.-H. Moeng, B. Stevens, D. H. Lenschow, and S. D. Mayor, 1998: 'Structure of the entrainment zone capping the convective atmospheric boundary layer', *J. Atmos. Sci.*, **55**, 3042–3064.

Weaver, C. P. and R. Avissar, 2001: 'Atmospheric disturbances caused by human modification of the landscape', *Bull. Amer. Meteorol. Soc.*, **82, 2**, 269–281.

Willis, G. E. and J. W. Deardorff, 1974: 'A laboratory model of the unstable planetary boundary layer', *J. Atmos. Sci.*, **31**, 1297–1307.

List of Figures

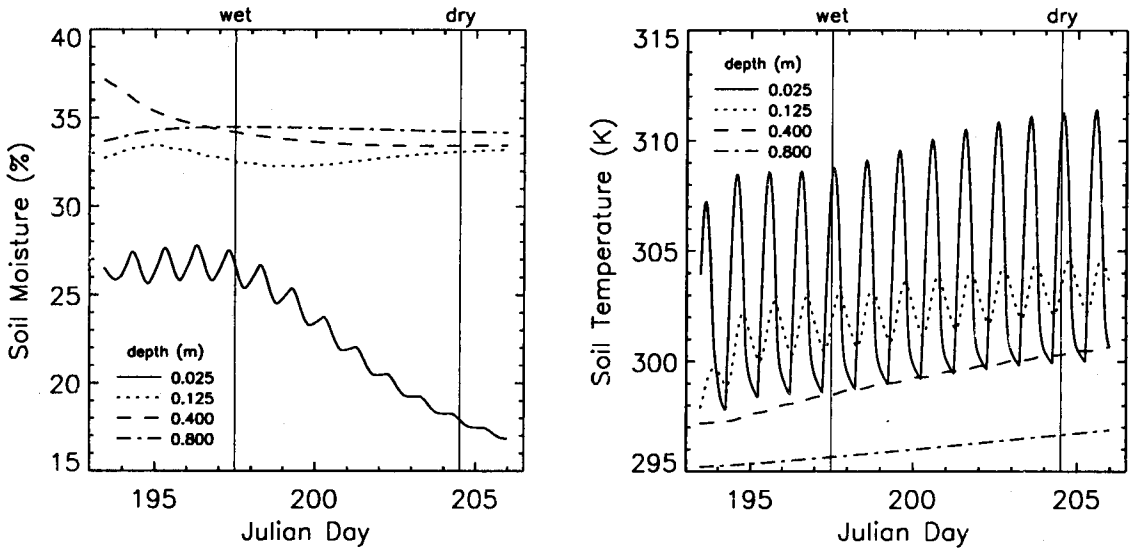

Figure 1: Time evolution of the four vertical levels of soil moisture and temperature from the 1-D off-line LSM run initialized from measurements from Little Washita at 11:30 LST on Day 193 of SGP97. Initial soil conditions for the LSM for the *wet* and *dry* coupled simulations are taken at noon seven days apart.

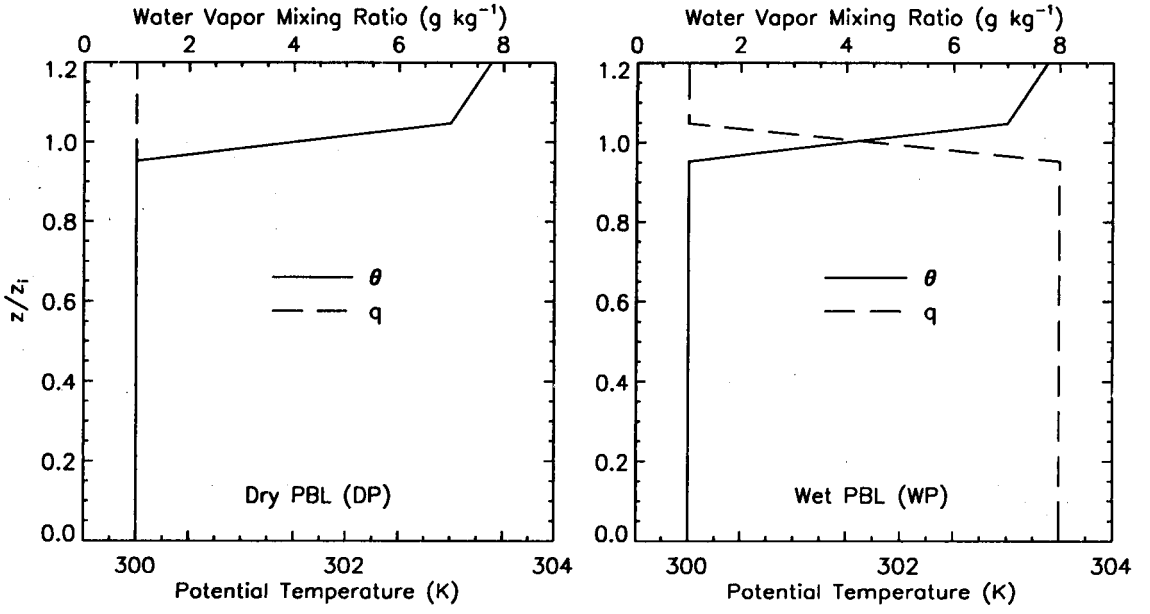

Figure 2: Initial profiles of potential temperature (θ) and water vapor mixing ratio (q) for the dry PBL (DP) and wet PBL (WP) cases.

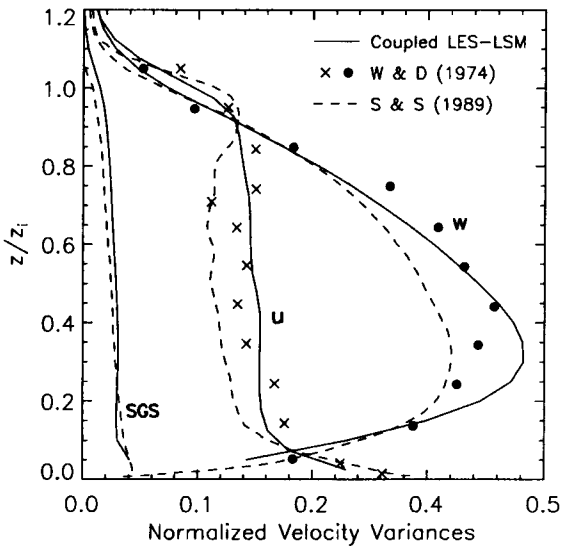

Figure 3: Comparison of velocity variances ($\mathbf{u} = \langle u''^2 + \frac{2}{3}e\rangle/w_*^2$, $\mathbf{w} = \langle w''^2 + \frac{2}{3}e\rangle/w_*^2$, and $\mathbf{SGS} = \frac{2}{3}\langle e\rangle/w_*^2$) derived from the current coupled LES-LSM code (solid lines) and those measured in the tank experiments of Willis and Deardorff (1974) case S1 (×,•) and the LES results of Schmidt and Schumann (1989) (dashed line). Note that the bold typeface does not imply a vector quantity. The SGS energy (e) predicted by the LES is assumed isotropic such that one-third is added to each of velocity variances.

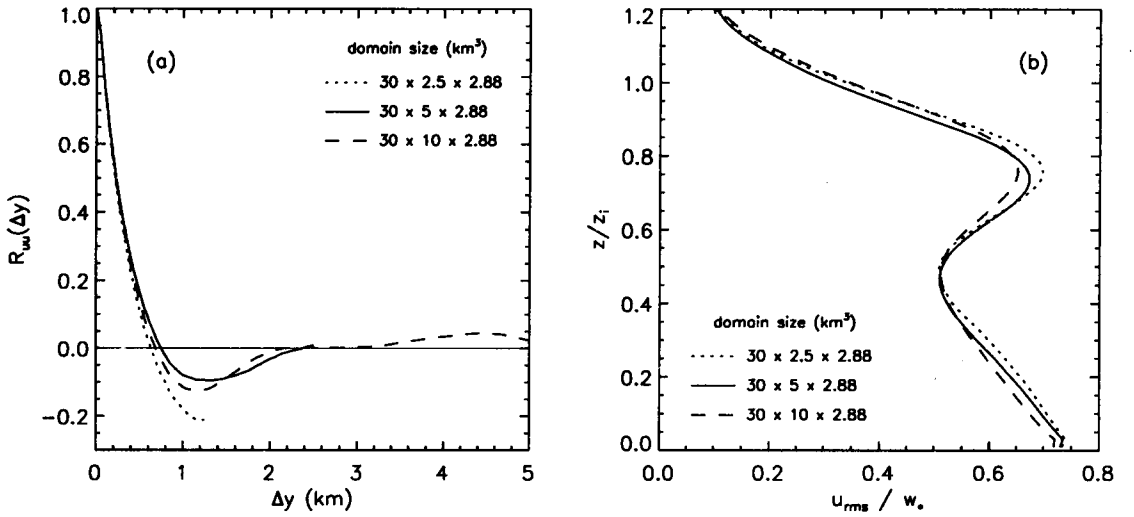

Figure 4: Comparison of horizontal velocity two-point correlations $[R_{uu}(\Delta y)]$ versus increasing lag in the lateral direction (Δy) for three cases that are identical to case DP-15S except for the lateral extent of the domain. The second panel depicts vertical profiles of the square root of the horizontally- and time-averaged horizontal velocity variance normalized by w_* for the same three cases.

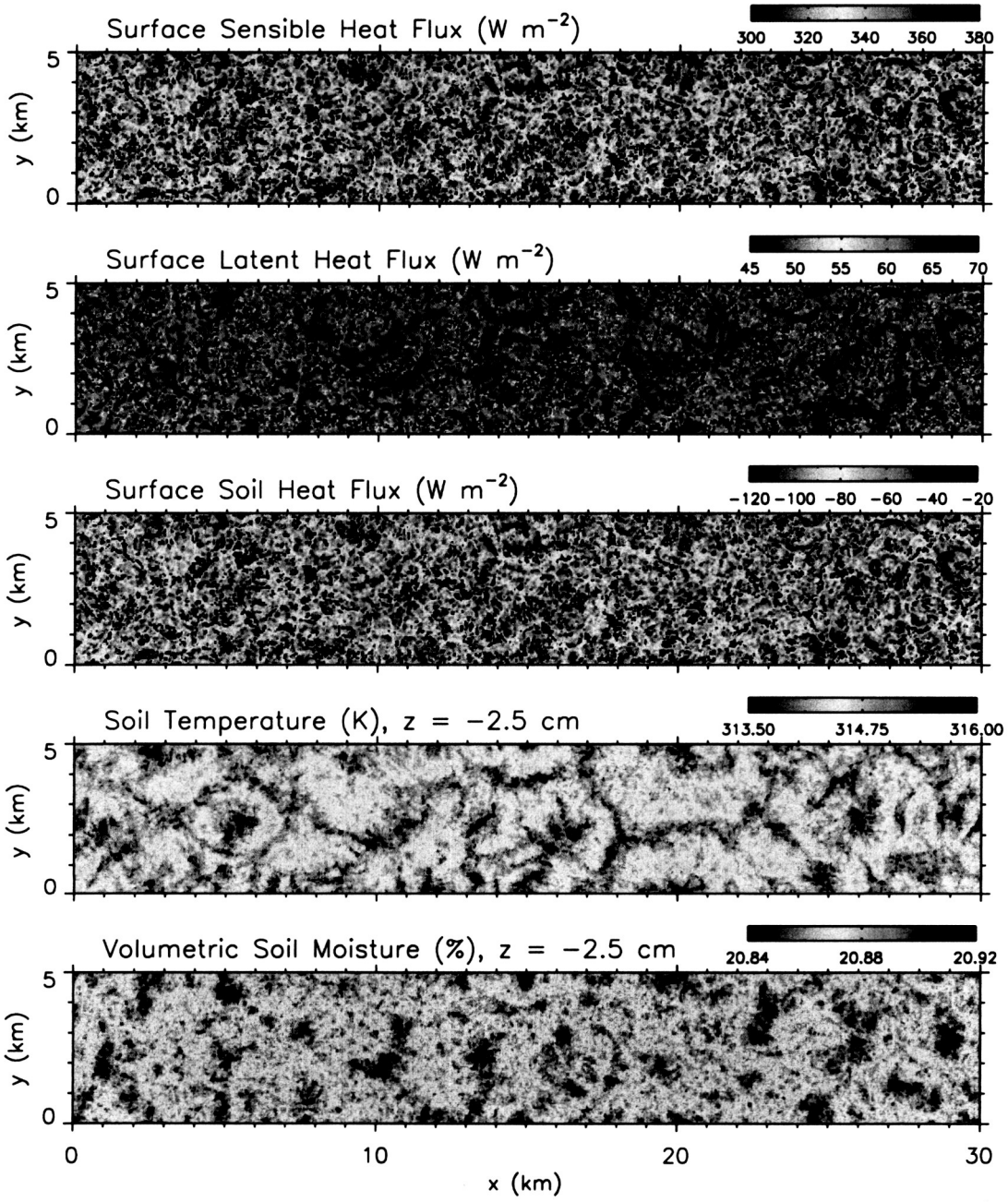

Figure 5: Instantaneous (x,y) slices of surface fluxes (sensible, latent and soil heat fluxes) and the corresponding soil temperature and moisture at the uppermost vertical level in the LSM (z = - 2.5 cm, which represents the vertical average over the top five centimeters in the soil) from DP-AS at the last time step in the simulation.

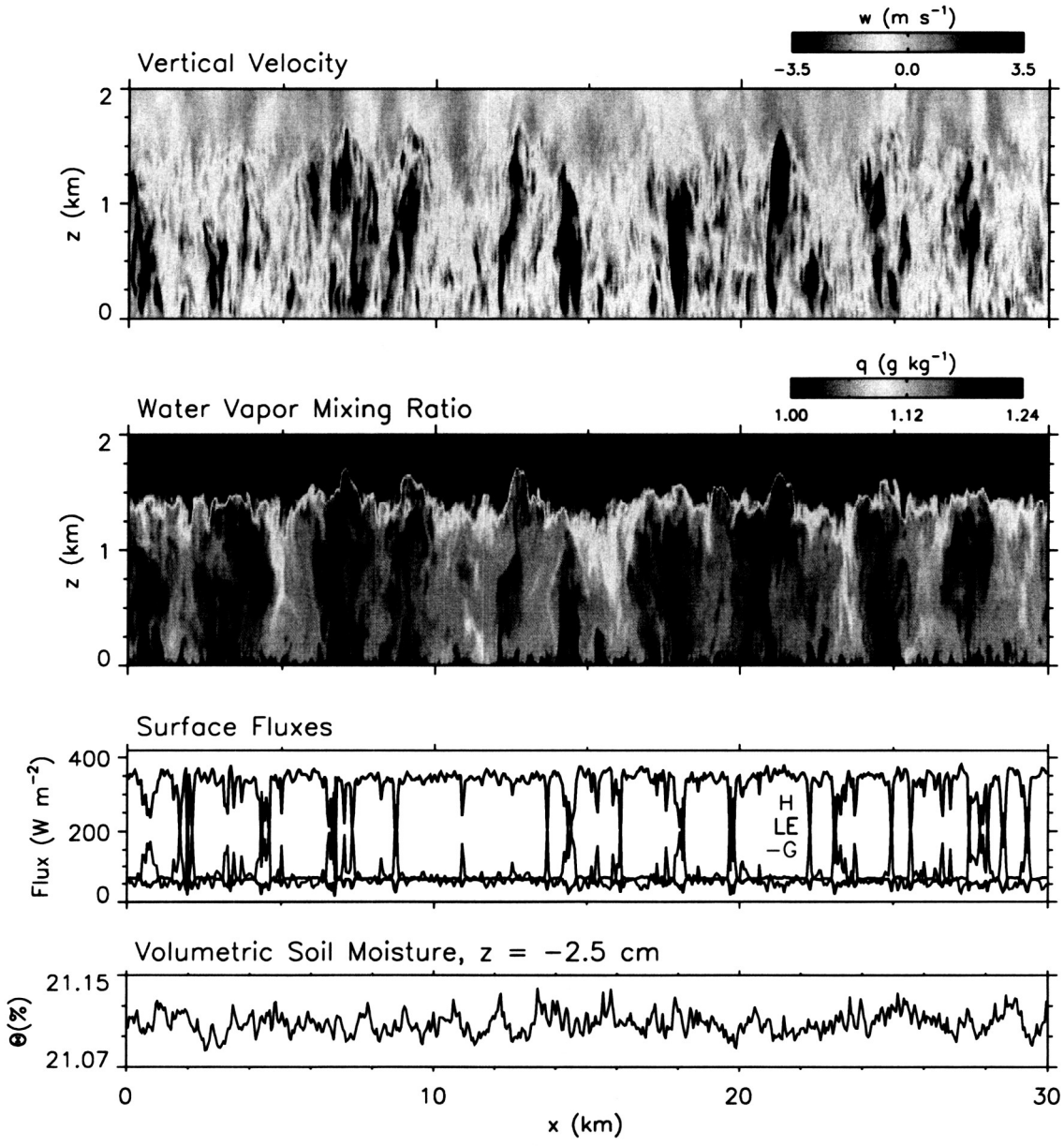

Figure 6: Instantaneous two dimensional slices of vertical velocity and water vapor mixing ratio at the first time step used in the averaging for case DP-AS (top two panels). The third panel depicts the coincident surface forcing (H, LE, -G) determined via the LES-LSM coupling. The lowest panel is the volumetric soil moisture at the uppermost soil level, z = - 2.5 cm.

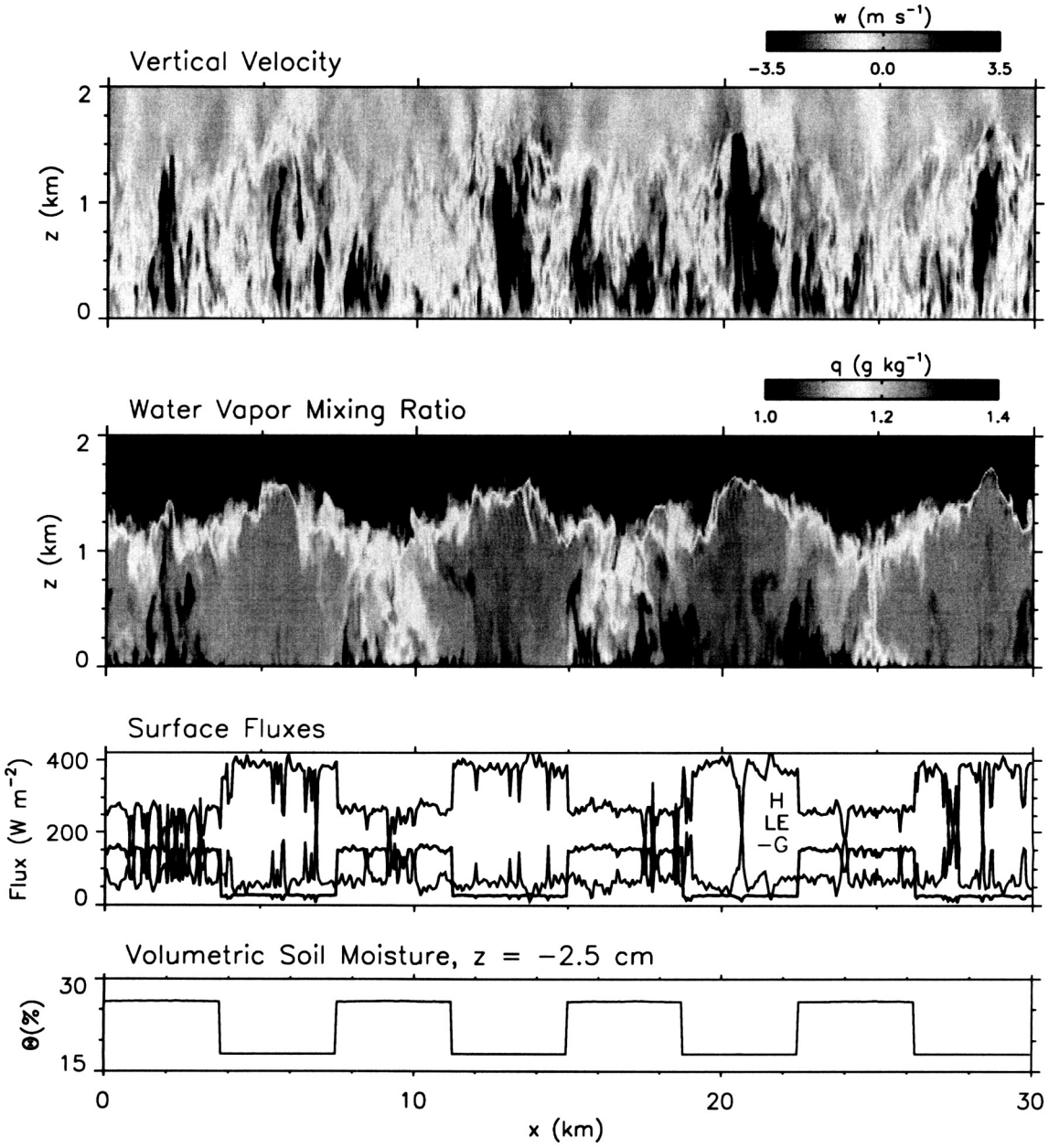

Figure 7: The same as Figure 6, except for case DP-7.5S.

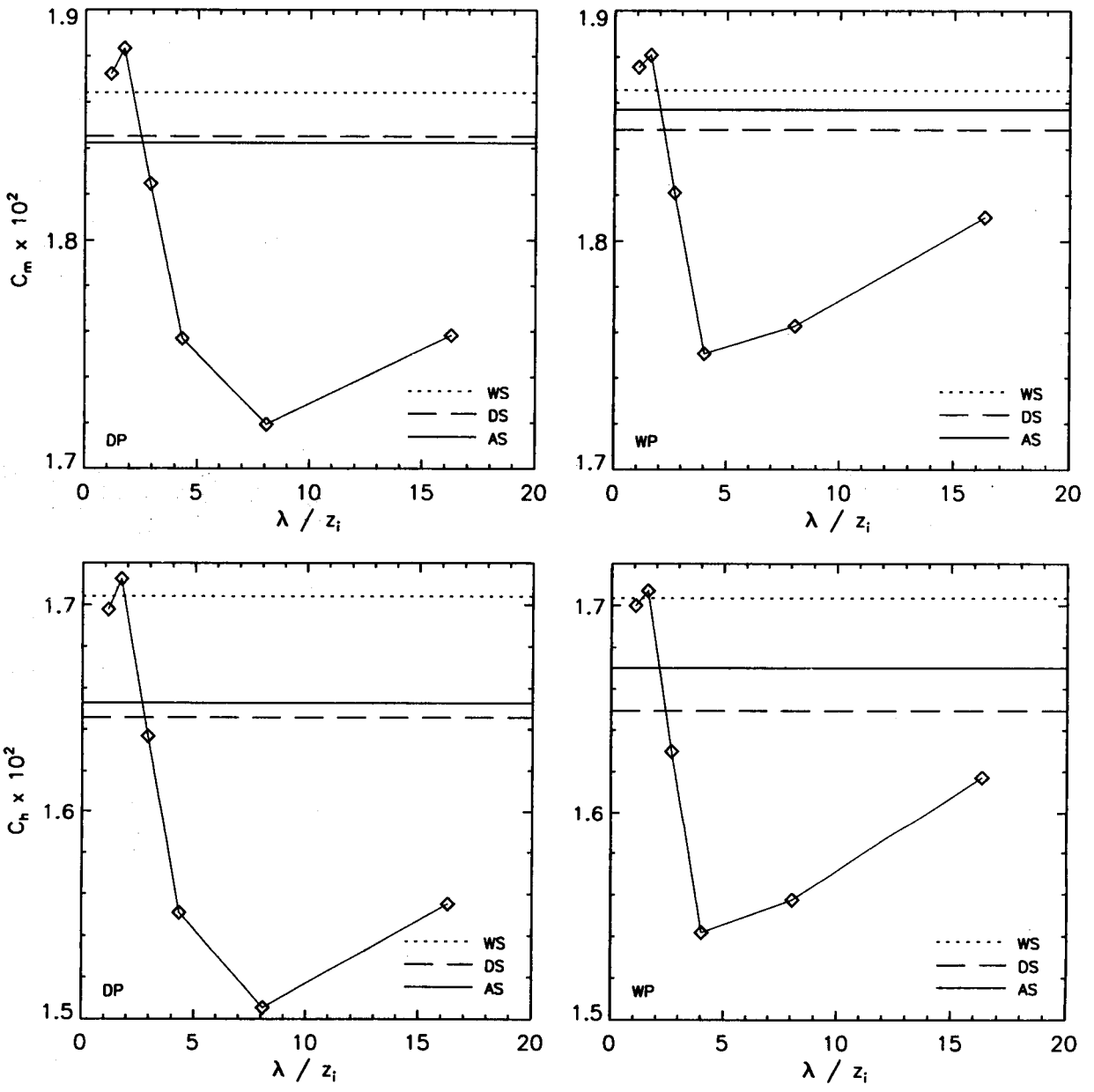

Figure 8: Variation of the horizontally- and time-averaged surface exchange coefficients for momentum and heat (C_m and C_h) versus the normalized heterogeneity wavelength (λ/z_i) for both the DP and WP cases. The line with symbols represents the heterogeneous soil cases. The solid, dashed and dotted lines with no symbols are the homogeneous soil cases.

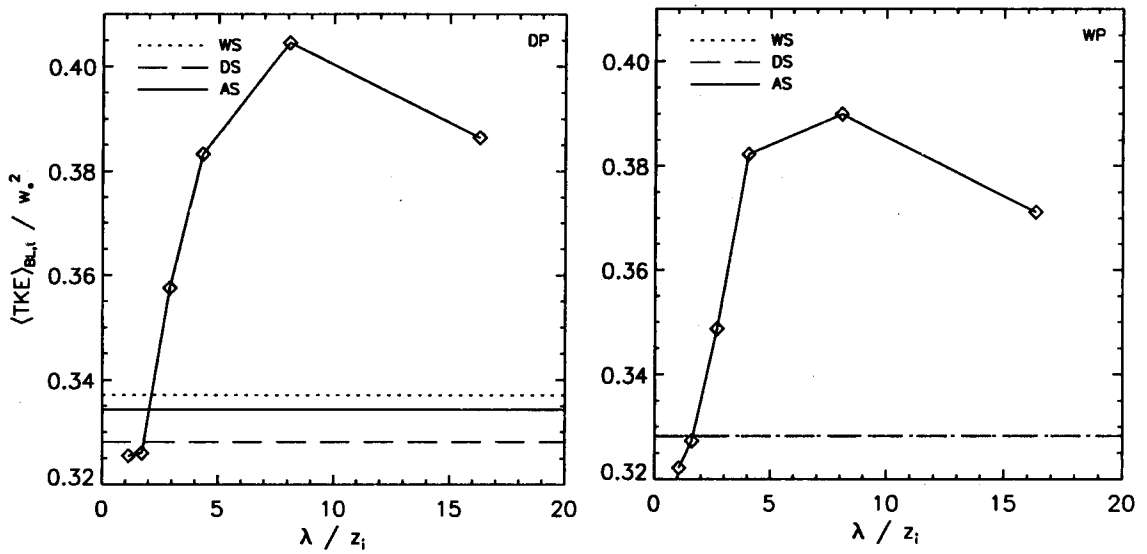

Figure 9: Boundary-layer and time averaged turbulence kinetic energy normalized by w_*^2 versus the normalized heterogeneity wavelength (λ/z_i) for both the DP and WP cases. The line with symbols represents the heterogeneous soil cases. The solid, dashed and dotted lines with no symbols are the homogeneous soil cases.

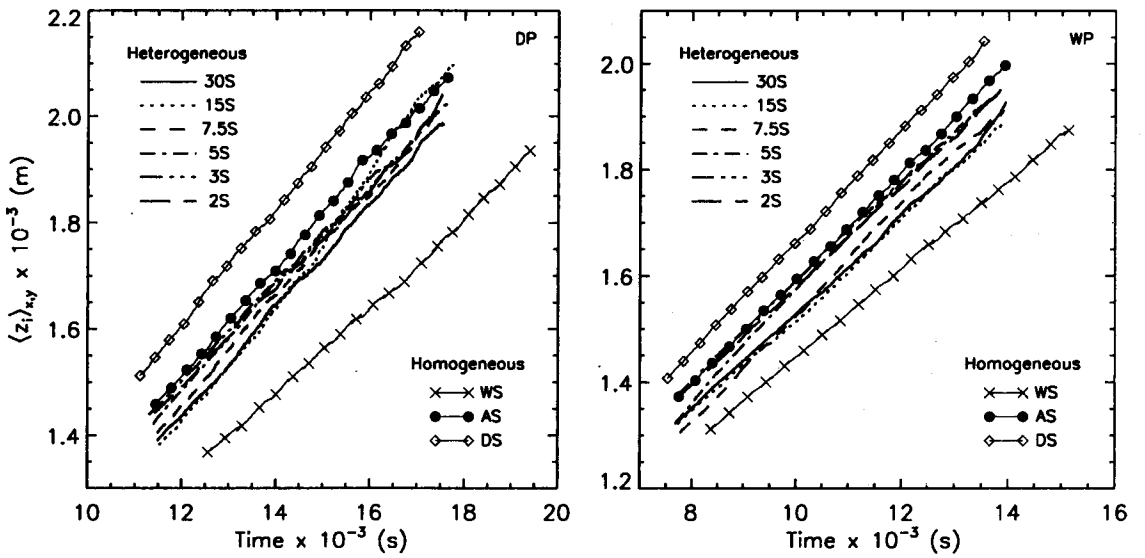

Figure 10: Time evolution of the horizontally averaged boundary layer height (z_i) for all cases over the complete averaging period for both the DP and WP cases. Lines by themselves represent heterogeneous cases. Lines with symbols represent homogeneous cases.

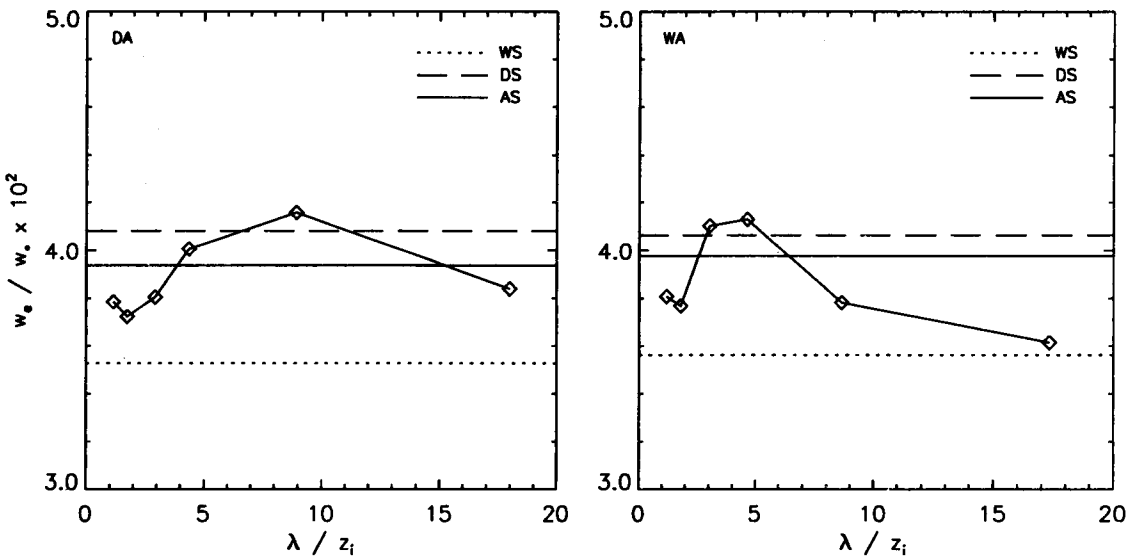

Figure 11: Normalized entrainment rates (w_e/w_*) versus the normalized heterogeneity wavelength (λ/z_i) for both the DP and WP cases. The line with symbols represents the heterogeneous soil cases. The solid, dashed and dotted lines with no symbols are the homogeneous soil cases.

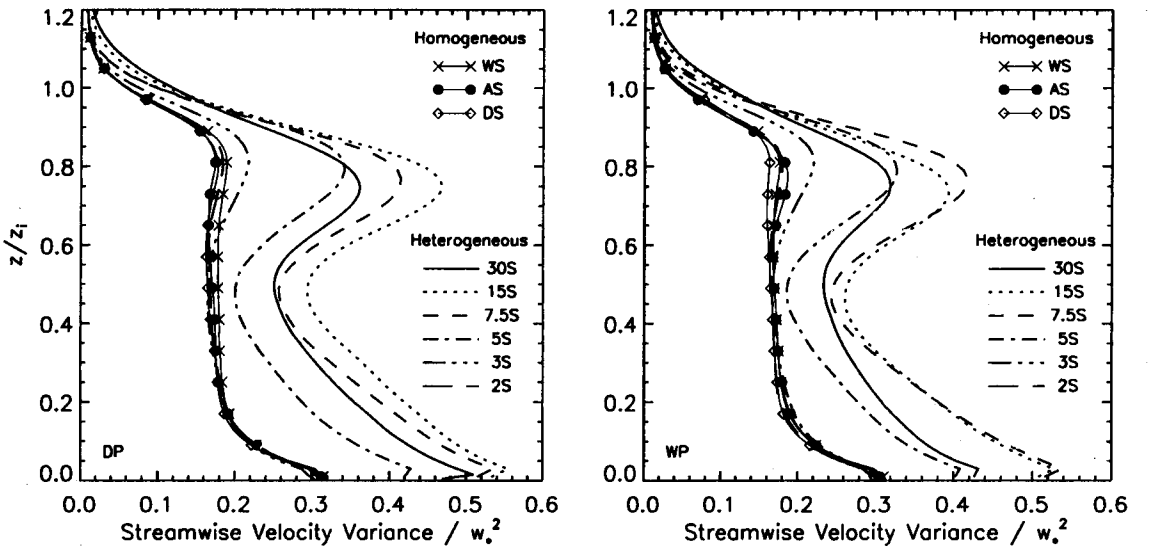

Figure 12: Vertical profiles of normalized horizontal velocity variance, $(\langle u''^2 \rangle + \frac{2}{3}\langle e \rangle)/w_*^2$, for both the DP and WP cases. Lines by themselves represent heterogeneous cases. Lines with symbols represent homogeneous cases. The variable e is the subgrid-scale energy as predicted by the LES.

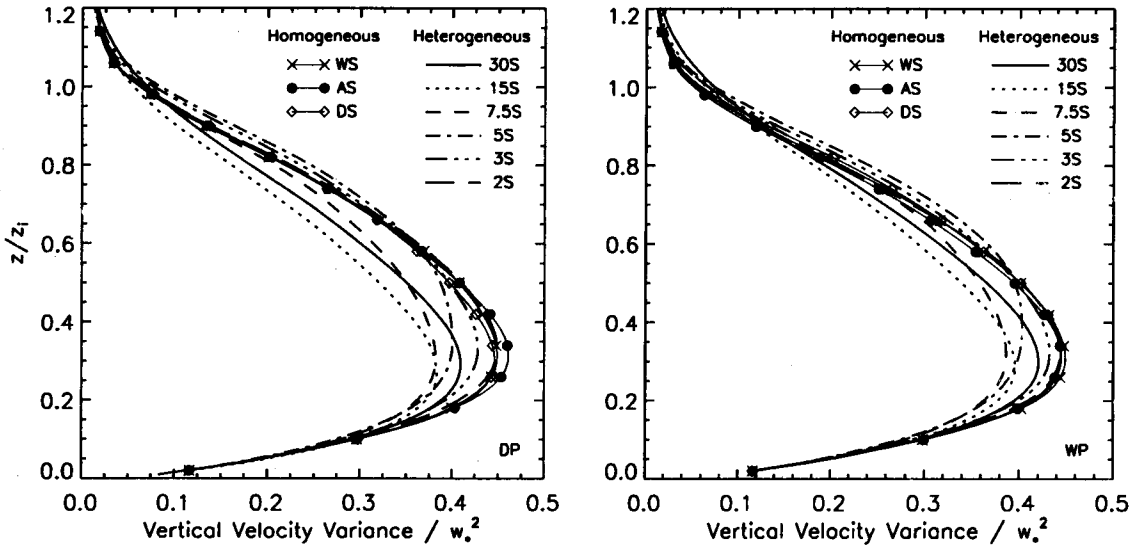

Figure 13: Vertical profiles of normalized vertical velocity variance, $(\langle w''^2 \rangle + \frac{2}{3}\langle e \rangle)/w_*^2$, for both the DP and WP cases. Lines by themselves represent heterogeneous cases. Lines with symbols represent homogeneous cases.

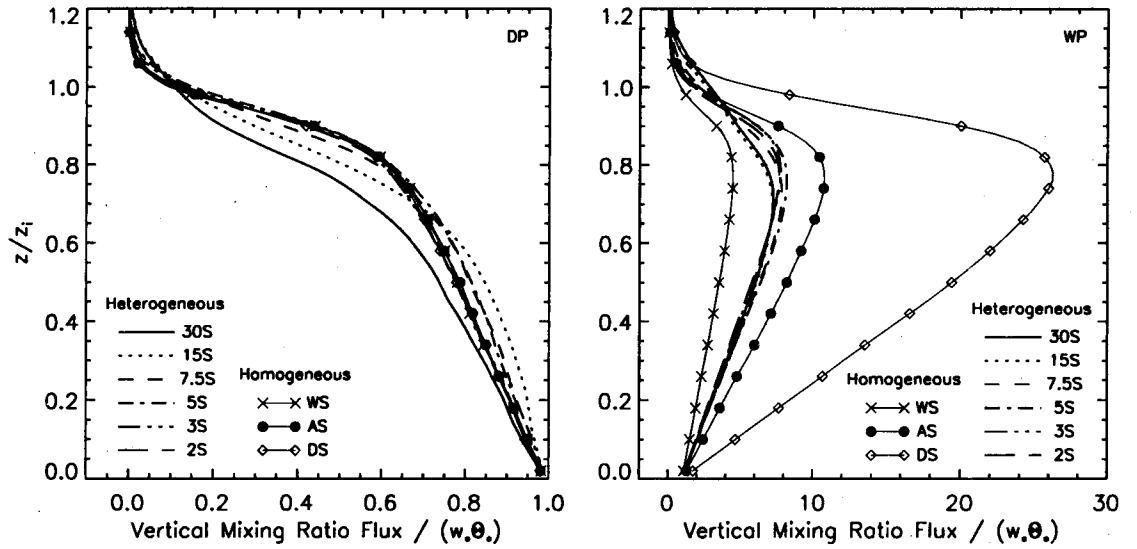

Figure 14: Vertical profiles of normalized vertical flux of water vapor mixing ratio ($\langle w''q'' + \tau_{wq} \rangle / (w_* \Theta_*)$) for both the DP and WP cases. Lines by themselves represent heterogeneous cases. Lines with symbols represent homogeneous cases. τ_{wq} is the subgrid-scale vertical mixing ratio flux predicted by the subgrid-scale model.

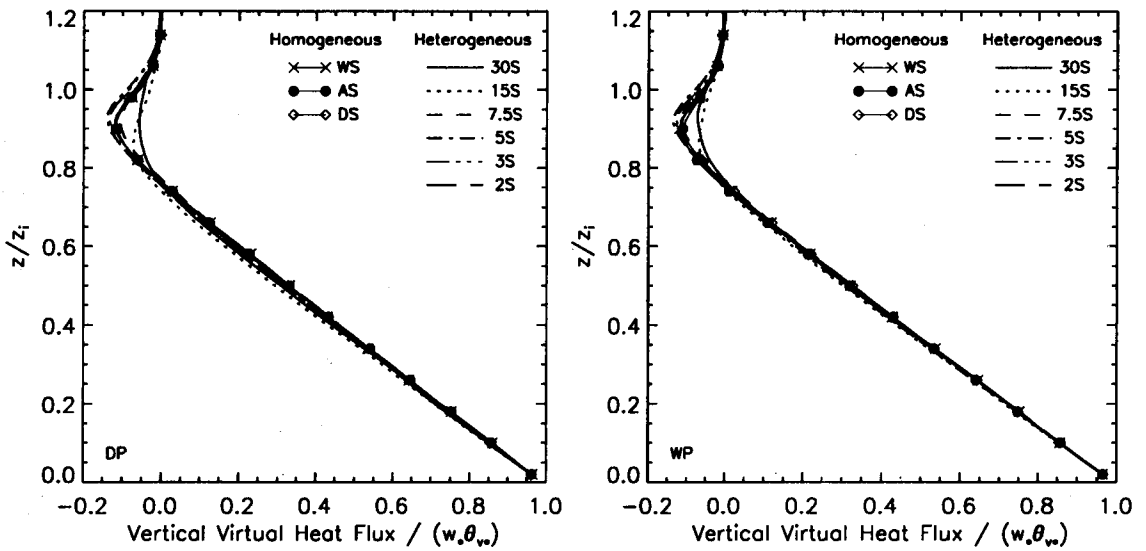

Figure 15: Vertical profiles of normalized vertical flux of virtual potential temperature ($(\langle w''\theta_v'' + \tau_{w\theta_v}\rangle/(w_*\theta_{v*})$) for both the DP and WP cases. Lines by themselves represent heterogeneous cases. Lines with symbols represent homogeneous cases. $\tau_{w\theta_v}$ is the subgrid-scale vertical virtual potential temperature flux predicted by the subgrid-scale model.

List of Tables

Case	z_i (km)	λ/z_i	w_* (m s^{-1})	H (W m^{-2})	LE (W m^{-2})	G (W m^{-2})	θ_{v*} ($m\ K\ s^{-1}$)	β
DP-WS	1.66	n/a	2.35	259.42	138.97	80.98	0.23	1.87
DP-DS	1.85	n/a	2.69	358.74	25.32	78.22	0.32	14.17
DP-AS	1.79	n/a	2.58	326.70	59.91	81.26	0.29	5.45
DP-30S	1.71	17.55	2.52	311.00	83.41	77.82	0.27	3.73
DP-15S	1.75	8.56	2.54	312.61	84.30	76.46	0.28	3.71
DP-7.5S	1.73	4.33	2.52	310.51	83.94	78.59	0.27	3.70
DP-5S	1.72	2.91	2.51	308.05	82.97	80.90	0.27	3.71
DP-3S	1.74	1.72	2.51	307.14	82.56	80.94	0.27	3.72
DP-2S	1.74	1.15	2.51	308.05	82.86	79.83	0.27	3.72
WP-WS	1.67	n/a	2.37	264.72	133.73	80.68	0.23	1.98
WP-DS	1.79	n/a	2.67	361.68	23.77	77.20	0.32	15.22
WP-AS	1.76	n/a	2.58	329.94	56.80	81.12	0.29	5.81
WP-30S	1.70	17.61	2.52	315.22	79.73	76.92	0.28	3.95
WP-15S	1.70	8.82	2.52	316.11	80.53	75.96	0.28	3.93
WP-7.5S	1.72	4.37	2.53	315.62	80.78	76.69	0.28	3.91
WP-5S	1.72	2.91	2.52	312.61	79.76	79.71	0.28	3.92
WP-3S	1.72	1.74	2.52	311.43	78.88	80.48	0.28	3.95
WP-2S	1.73	1.55	2.52	312.05	79.02	79.73	0.28	3.95

Table 1: Bulk properties for all cases. The quantities are: z_i, the PBL height; λ/z_i, the ratio of the scale of the heterogeneity (λ) to the PBL height; w_*, the convective velocity; H, the surface sensible heat flux ($= \rho C_p w_* \theta_*$); LE, the surface latent heat flux ($= \rho L w_* \Theta_*$); G, the soil heat flux; θ_{v*}, the total surface buoyancy flux ($= \langle w''\theta'' \rangle + 0.61\,\theta_o \langle w''q'' \rangle$); β, the Bowen ratio (H/LE). These bulk quantities are averaged horizontally over all space and over the entire averaging period. The angle brackets denoting this averaging process are omitted for convenience. *n/a* stands for *not applicable* since λ is undefined for the homogeneous cases.